Improvement of the Electrochemical Hydrogen Storage Performance of Mg-Based Alloys by the Various Partial Replacement Elements

M. Anik, G. Özdemir

This document appeared in

Detlef Stolten, Thomas Grube (Eds.):
18th World Hydrogen Energy Conference 2010 - WHEC 2010
Parallel Sessions Book 4: Storage Systems / Policy Perspectives, Initiatives and Co-operations
Proceedings of the WHEC, May 16.-21. 2010, Essen
Schriften des Forschungszentrums Jülich / Energy & Environment, Vol. 78-4
Institute of Energy Research - Fuel Cells (IEF-3)
Forschungszentrum Jülich GmbH, Zentralbibliothek, Verlag, 2010
ISBN: 978-3-89336-654-5

Improvement of the Electrochemical Hydrogen Storage Performance of Mg-Based Alloys by the Various Partial Replacement Elements

Mustafa Anik, **Gizem Özdemir**, Eskisehir Osmangazi University, Metallurgical and Materials Eng. 26480, Eskisehir, Turkey

1 Introduction

Mechanically alloyed Mg-based hydrogen storage alloys attract great attention as the negative electrodes for the nickel–metal hydride (Ni/MH) rechargeable batteries which have considerable potential for the utilization in cordless tools and electric vehicles [1-8]. The large scale practical applications, however, can only be possible if these alloys could be developed with the superior rate capabilities.

Modification of the alloy composition by the partial replacement of Mg is a common practice to improve the electrode performance of the Mg-based alloys [9]. In this work, as the continuation of our attempts to develop a high performance Mg-based negative electrode alloy by the composition modifications [9-13], MgNi, $Mg_{0.9}Zr_{0.1}Ni$, $Mg_{0.9}Ti_{0.1}Ni$ and $Mg_{0.9}Al_{0.1}Ni$ alloys were synthesized by mechanical alloying and the effects Zr, Ti and Al replacement elements on the electrochemical hydrogen storage characteristics of MgNi alloy were observed .

2 Materials and Methods

Elemental Mg, Ni, Ti, Zr and Al powders were mixed in various compositions and charged into the stainless steel vials under the high purity Ar atmosphere. The diameter of the stainless steel balls was 5 mm and the ball to powder weight ratio was selected as 20:1. The mechanical alloying was performed with a planetary ball mill and the milling speed was 500 rpm. The ball milling duration was selected as 25 h. The mechanical alloying was carried out by milling for 30 min in the forward direction then cooling for 15 min and then milling for 30 min in the reverse direction.

The phase structure of the alloy powders was examined by the X–ray diffractometer (Bruker axs D8) using Cu Kα radiation. The powder morphologies were observed by ZEISS SUPRATM 50 VP Scanning Electron Microscope (SEM). The size of the powders was measured by Model ALV CGS-3 compact goniometry system (dynamic light scattering).

Working electrodes were prepared by mixing 0.2 g alloy powder with 0.6 g nickel powder and then cold pressing into pellets of 10 mm in diameter, under a pressure of 10 ton cm^{-2}. $NiOOH/Ni(OH)_2$ counter electrode and a Hg/HgO reference electrode were used to set up a three-electrode cell in 6 M KOH solution. Tests were performed with PARSTAT Model 2273 potentiostat/galvanostat unit. The charge current density was 100 mA g^{-1} and the charging

was carried out down to the severe gassing potential. The discharge current density was 25 mA g^{-1} and the discharge cut-off potential was -0.6 $V_{Hg/HgO}$.

3 Experimental Results and Discussion

3.1 The structural and morphological characteristics

The overlaid XRD patterns of MgNi, $Mg_{0.9}Zr_{0.1}Ni$, $Mg_{0.9}Ti_{0.1}Ni$ and $Mg_{0.9}Al_{0.1}Ni$ alloys are shown in Figure 1. All the alloys give almost the same pattern with a broad peak around 41.5° which can be assigned to amorphous structure (or to the mixture of amorphous/nano-crytalline structure). The peaks for any particular structure and for any element in each alloy could not be observable in Figure 1.

The typical powder morphology of 25 h milled alloys is illustrated in the scanning electron micrograph in Figure 2a. The fragmentation of the coarse, cold-welded particles into the fine powders in these figures shows the typical morphology of the powders synthesized by the ball milling. The size distribution of the disintegrated particles of 25 h milled alloys is provided in Figure 2b. The average radius of the particles looks approximately 0.9 micron in Figure 2b.

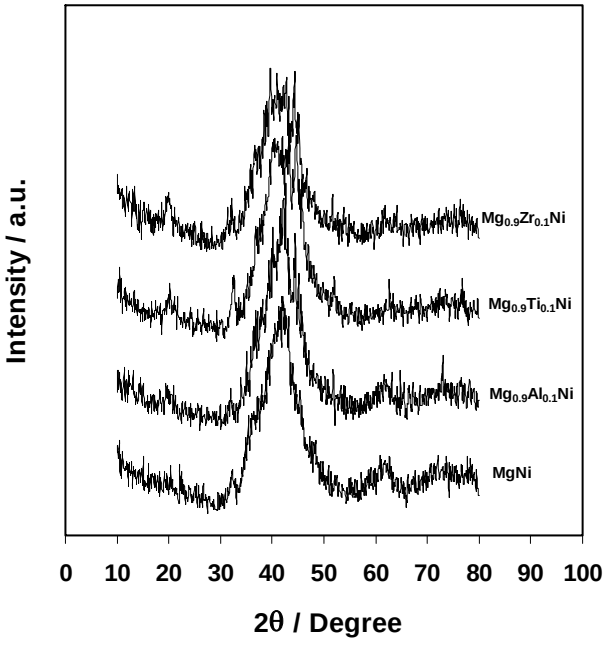

Figure 1: Overlaid XRD patterns of the alloys synthesized by 25 h milling.

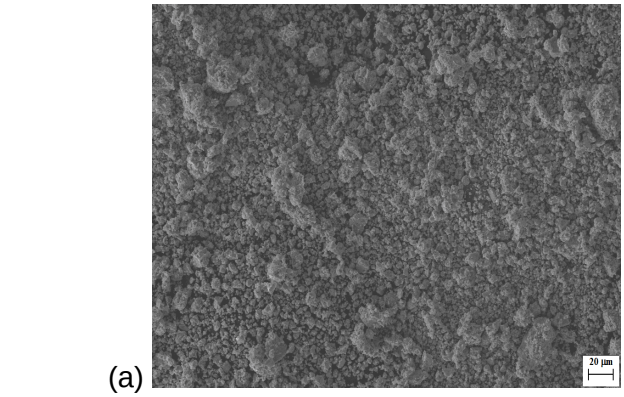

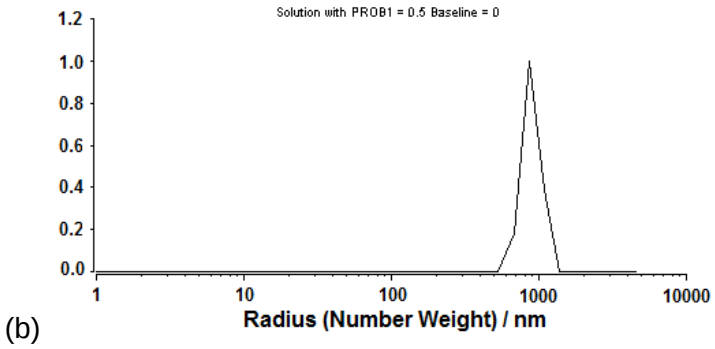

Figure 2: (a) Typical powder morphology and (b) powder size distribution of the alloys.

3.2 The cycle stability of the alloys

The variations in the discharge capacities of 25 h milled MgNi, $Mg_{0.9}Zr_{0.1}Ni$, $Mg_{0.9}Ti_{0.1}Ni$ and $Mg_{0.9}Al_{0.1}Ni$ alloys depending on the charge/discharge cycle numbers are depicted in Figure 3. The cyclic stabilities of the alloys are also evaluated by observing the capacity retaining rates, which are defined as $C_n/C_{max.}$ x 100% ($C_{max.}$ is the initial discharge capacity and C_n is the discharge capacity at n^{th} charge/discharge cycle), as in Figure 4.

The initial discharge capacities of MgNi, $Mg_{0.9}Zr_{0.1}Ni$, $Mg_{0.9}Ti_{0.1}Ni$ and $Mg_{0.9}Al_{0.1}Ni$ alloys were 495, 507, 491 and 403 mA h g^{-1}, respectively. Zirconium increases the initial discharge capacity slightly in Figure 3. In fact, the big-size Zr atoms (Mg = 1.72 A°, Ni = 1.62 A°, Zr = 2.16 A°) can create extra sites for the hydrogen storage in the alloy crystal structure and thus the alloy capacity increases. The cyclic performance of the alloy in the presence of Zr, however, did not show considerable improvement in Figure 4 ($Mg_{0.9}Zr_{0.1}Ni$ alloy keeps 52% of its initial capacity at 10^{th} charge-discharge cycle). The alloy cyclic performance increases significantly in the presence of Ti replacement element. While MgNi keeps 48% of its initial capacity, $Mg_{0.9}Ti_{0.1}Ni$ alloy keeps at least 70% of its initial discharge capacity at 10^{th} charge-discharge cycle in Figure 4. It is believed that Ti segregates to the surface and makes the alloy surface more penetrable by atomic hydrogen during the alloy cycling [14]. Although $Mg_{0.9}Al_{0.1}Ni$ alloy has low initial discharge capacity, the capacity retention rate of this alloy is acceptable. The capacity retention rate of Al-including alloy was 60% at 10^{th} charge-discharge cycle in Figure 4. This positive contribution of Al replacement element is generally attributed to the selective dissolution of the disseminated Al_2O_3 throughout the barrier

$Mg(OH)_2$ surface layer [9,10]. The selective dissolution makes the barrier hydroxide layer porous and more permeable for hydrogen, and thus the alloy cyclic stability gets better.

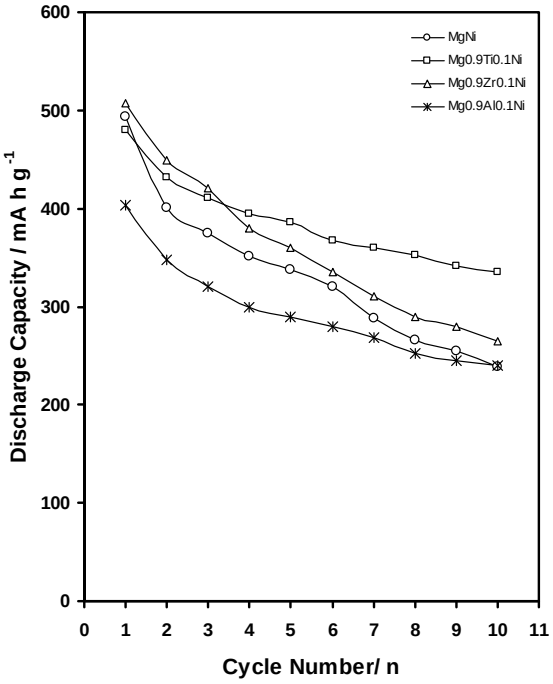

Figure 3: Discharge capacities as a function of cycle number.

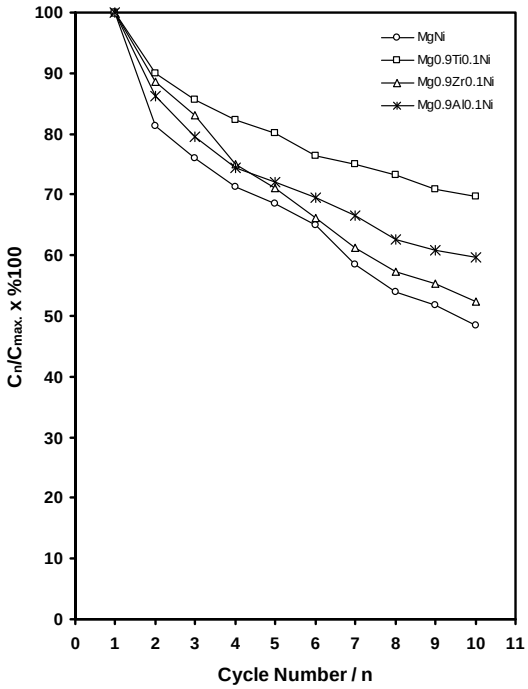

Figure 4: Cyclic stability as a function of cycle number.

References

[1] P. Selvam, B. Viswanathan, C.S. Swamy, V. Srinivasan, Int. J. Hydrogen Energy 11 (1986) 169-192.

[2] N. Cui, B. Luan, H.K. Liu, H.J. Zhao, S.X. Dou, J. Power Sources 55 (1995) 263-267.

[3] L. Zaluski, A. Zaluska, J.O. Ström-Olsen, J. Alloys Comp. 217 (1995) 245-249.

[4] S. Orimo, H. Fujii, Intermetallics 6 (1998) 185-192.

[5] N. Cui, P. He, J.L. Luo, Acta Mater. 47 (1999) 3737-3743.

[6] M. Dornheim, S. Doppiu, G. Barkhordarian, U. Boesenberg, T. Klassen, O. Gutfleisch, R. Bormann, Scripta Mater. 56 (2007) 841-846.

[7] M. Jurczyk, L. Smardz, I. Okonska, E. Jankowska, M. Nowak, K. Smardz, Int. J. Hydrogen Energy, 33 (2008) 374-380.

[8] X. Zhao, L. Ma, Int. J. Hydrogen Energy 34 (2009) 4788-4796.

[9] M. Anik, J. Alloys Comp. 486 (2009) 109-114.

[10] M. Anik, H. Gasan, S. Topcu, I. Akay, N. Aydinbeyli, Int. J. Hydrogen Energy, 34 (2009) 2692-2700.

[11] M. Anik, I. Akay, S. Topcu, Int. J. Hydrogen Energy 34 (2009) 5449-5457.

[12] M. Anik, I. Akay, G. Ozdemir, B. Baksan, Int. J. Hydrogen Energy 34 (2009) 9765-9772.

[13] M. Anik, J. Alloys Comp. 491 (2010) 565-570.

[14] J.J. Jiang, M. Gasik, J. Power Sources 89 (2000) 117-124.